Solid Freeform Fabrication 2021: Proceedings of the 32nd Annual International
Solid Freeform Fabrication Symposium – An Additive Manufacturing Conference
Reviewed Paper

BIMETALLIC CASTINGS FOR WEAR PERFORMANCE THROUGH INFILTRATION OF ADDITIVE MANUFACTURED METAL LATTICE STRUCTURES

J. C. Liggett[1], D. A. Snelling[1], M. Xu[2], O. J. Myers[3], and S. M. Thompson[4]

[1]Department of Manufacturing Engineering, Georgia Southern University, Statesboro, GA 30460

[2]Department of Mechanical Engineering, Georgia Southern University, Statesboro, GA 30460

[3]Department of Mechanical Engineering, Clemson University, Clemson, SC 29631

[4]Alan Levin Department of Mechanical and Nuclear Engineering, Kansas State University, Manhattan, KS 66506

Abstract

High chromium white iron is an alloy frequently employed in the production of abrasion resistive wear components. Ground engaging components for mining or earthmoving frequently require such materials, as well as slurry pumps for mining applications. Although high chromium white iron alloy demonstrates excellent wear performance due to the formation of chromium carbides, it is brittle and lacks toughness. Impact resistance is often of great importance for ground engaging wear components; hence, this study will investigate a method by which high chromium white iron wear components may be reinforced by the formation of a bimetallic composite. In this research, an additively manufactured lattice structure of 316L stainless steel is infiltrated with high chromium white iron via the metal casting process. This procedure results in a bimetallic casting of reinforced white iron. Complete infiltration and metallurgical diffusion bonding were observed between the two alloys, validating this method as a means of reinforcing high chromium white iron castings for applications requiring high abrasion and impact resistance.

Introduction

Alloy selection for metal components is often a compromise between desired material properties which are typically mutually exclusive. Applications requiring both high toughness and high wear resistance in metal alloy components often lead to significant compromise, as high hardness is advantageous for wear resistance but can result in a brittle material with low toughness [1]. Because desired material property combinations can be mutually exclusive within most engineering alloys, much development has been done recently to develop bimetal composites which can blend the strengths of two different alloys to make up for the weaknesses of each.

The majority of the research and development in this area has been focused on bimetal casting techniques, in which conventional metal casting techniques are used to produce a composite through pouring successive layers of different molten alloys into a mold cavity, or by pouring a liquid metal alloy onto a solid metal substrate. [2–12] However, little has been done to study the applications of advanced additive manufacturing techniques in the development of bimetal castings. This study will seek to fill this gap by examining the feasibility of creating a bimetal composite through a hybrid casting-additive manufacturing process.

Existing work has been performed exclusively examining the casting process in the development of bimetallic wear components. In separate studies performed by Zic et al. and Zhu et al., the viability of bimetallic casting techniques involving the pouring of successive layers of liquid metal alloys is explored. [4, 5] In both cases, a wear resistant white iron alloy is coupled with a ductile steel to improve the impact response of the casting. In another study, Wróbel examines the feasibility of producing a bimetallic composite by pouring a liquid metal alloy over a solid metal substrate. [6] These studies each provide important insight into the application of metal casting techniques toward bimetallic composite production.

While much has been done to examine the production of bimetal composites through metal casting techniques, little work has been performed examining the applications of additive manufacturing in further developing bimetallic composite casting. Additive manufacturing can be used to create structures of high complexity with maximum material efficiency, low tooling cost, low labor cost, and low environmental impact [13]. Additive manufacturing (AM) of metal feed stock materials in particular has positively impacted a multitude of industries, being capable of producing complex end-use components with good surface finish without the complex processes involved in traditional manufacturing methods such as metal casting. AM has also been applied recently to the production of bimetallic composites in order to produce components of different compositions through a single manufacturing process. The thermal mismatch between materials in bimetallic AM has been overcome in some cases by a composition gradient in the transition zone in powder bed fusion processes, a process in which a metal feedstock powder is bonded through a laser or electron energy source to produce a final structure [13].

While new AM methods have provided the potential for bimetal component production, they fall short in a few key areas. First, metal AM components are limited by deposition rates and therefore cannot scale up beyond a certain point [14]. Thermal management is tied intrinsically to deposition rates and thus there is a maximum print volume in which powder bed fusion methods can operate successfully [14]. While other metal AM methods such as directed energy deposition offer the potential to overcome this size limitation, materials manufactured through such methods possess inherent microstructure flaws and crack defects which do not suite the material to high toughness or wear applications [14,15].

To best consider how AM methods may be used to improve bimetallic metal casting, it is important to examine areas in which AM techniques excel. One application for which AM is ideally suited is the production of complex lattice structures. Lattice or cellular structures can be seen throughout nature, featuring high strength, high stiffness, better energy absorption, and superior thermal and acoustic properties. [16] While these structures are desirable in many engineering applications, traditional manufacturing processes struggle to produce such complex geometric structures or incur high costs during production [16,17]. AM however excels at the production of complex cellular structures, and powder bed fusion techniques in particular offer the ability to produce high strength metal lattice structures with minimal production challenges [17,18].

Lattice structures excel at high strength to weight ratio applications because they are designed by placing material only where it is necessary [19]. Such structures can be designed as

either stochastic structures, which feature a randomly distribution of voids, or periodic structures, which feature ordered, repeated unit cell structures [17,19]. Periodic structures are often easier to design and control, as the overall shape can be broken down into predefined structural unit cells sometimes referred to as Manufacturable Elements [19]. These structural unit cells can be combined easily using element approximation methods to turn a solid part design into a lattice composed of unit cells of known structural properties, and thus the mechanical behavior of the lattice can be estimated [19]. Furthermore, lattice structures can be of uniform composition or can be hierarchical, in which the strut and cell dimensions change with location in the model. Examples of hierarchical lattice structures are often found in nature and are shown to improve overall structural performance [20].

In a study performed by Zhong et al., the implementation of periodic unit cell lattice structures in the production of lightweight structural components was examined. It was shown that the use of lattice structures was capable of reducing weight by 62%, compared to 54% reduction made possible by topology optimization alone [21]. Zhong et al. studied common cubic unit cell lattices, tetrakaidecahedron, diamond, and body-centered cubic structures. These shapes were composed of cylindrical struts, with study parameters varying with unit cell length, strut diameter, and lattice volume fraction. It was found that, given similar volume fractions and unit cell sizes, tetrakaidecahedron structures demonstrated significantly superior mechanical properties compared to diamond or body centered cubit structures. As found by this study, unit cell lattice structures offer key advantages over general topology optimization and special unit cell structures are ideally suited for high strength to weight ratio applications.

More complex lattice structures can be modeled through relative density mapping methods [22]. According to Alzahrani et al., the overall strength of a structural lattice is dictated by the volumetric density of the lattice [22]. The strengths of a lattice can be evaluated by calculating the deformation of the interconnecting strut network in the lattice. For this reason, when the volumetric density of the lattice is higher, more or thicker struts will be present which thereby increases the strength of the structure [22]. In Relative Density Mapping (RDM), the strength of the lattice is calculated by the volumetric density of finite elements within the lattice using a mathematical formula to correlate the strut size with each element's relative density.

Further advanced design techniques proposed by Wang et al. address limitations in lattice design [23]. As noted in this study, most design techniques do not evaluate the global optimized solution for the lattice. It is noted that determining the true global optimization is difficult due to disparity between the lattice structure distribution and the stress distribution in the structure and due to anisotropic material properties inherent in AM manufacturing techniques [23]. In this study, a method was developed which allowed for global optimization of a lattice structure through consideration of the principal stress lines through the component. Principal stress lines, orthogonal curve pairs which delineate the internal stress trajectory through a model, are shown to represent and support loading more efficiently than a grid-based approach [24]. A lattice structure is then created which conforms to the principal stress lines in the model.

Applications of AM lattice structures are numerous; with most structures being built using the laser-powder bed fusion (L-PBF) AM method. Zhao et al. demonstrated the ability of Ti-6Al-4V alloy lattice structures to absorb energy in high impact applications [25]. Gyroidal lattice

structures were shown to exhibit layer by layer failure in compression studies which allowed the load-bearing capability of the structure to increase during compression. Other studies show the ability of AM lattice structures to form lattice scaffolds for applications in tissue engineering [26] [27,28]. Large scale lattice structures for high strength to weight ratio structural applications were explored in a study performed by Yan et al. [18]. Selective laser melting AM methods were capable of producing gyroid lattice structures with unit cell size ranging up to 8mm.

While lattice structures produced through AM show significant applications in engineering design, such structures are not without draw-backs. In the same study which showed the viability of lattice structures with unit cells ranging up to 8mm in size, the yield strength and elastic modulus was observed to decrease with increasing unit cell size, indicating an upper limit to lattice unit cell sizing [18]. Additionally, the presence of porosity defects and rough surfaces in components made by metal AM methods is unavoidable, and can lead to poor fatigue performance [29,30]. Delamination defects are another inherent weakness of AM methods which can critically reduce material properties of AM components [31,32]. For this reason, there is significant room remaining for improving AM lattices for use in large scale structural applications.

In this study, the development of a bimetal composite is proposed which incorporates the recent development of AM lattice structures with the metal casting process. The L-PBF AM method will be used to produce a tetrakaidekahedron lattice structure of 316L Stainless steel with superior strength to weight ratios [16–18]. To prepare the material for high wear applications, such as those required for ground engaging components, high chromium white iron will be infiltrated into the lattice matrix through liquid-solid bimetal casting techniques to form a bimetallic composite of high hardness, wear resistant white iron reinforced by an interior lattice of high strength steel [5,7]. The fusion zone between the two materials will be examined through microstructure studies to determine the integrity of the composite bond. In this manner, a bimetallic composite will be examined which is produced using a hybrid manufacturing process blending metal additive methods with conventional casting techniques.

Alloy Development

The production of a bimetallic composite with a robust interface is heavily dependent on alloy development and selection. For this reason, the two alloys used in this composite should be carefully selected so that they exhibit the necessary individual material properties while also being highly compatible with each other. AM is the most heavily restricted manufacturing process in terms of alloy selection and thus the AM alloy will be selected first. As the casting process accepts a much wider range of alloy compositions, the cast alloy will be subsequently developed to compliment the choice of AM material. In this manner two alloys will be selected which promote complete fusion between the materials.

Stainless steel (SS) 316L was selected as the lattice structure material for L-PBF due to its excellent additive manufacturability, corrosion resistance, low cost, and availability. This is a high alloy stainless steel which features up to 18 wt% Cr, which gives it excellent corrosion resistance necessary for ground engaging applications [33]. 316L stainless is additionally considered to be a weldable steel, featuring good resistance to carbide formation in the fusion zone [33]. The high chromium content of 316L also makes it a good match with high Cr white iron, as Cr diffusion

from the stainless steel will enhance the properties of the infiltration alloy rather than detract from them.

High Cr white iron was selected as the infiltration alloy in this experiment; however, flexibility exists in the exact chemistry of the alloy. To determine the exact composition of white iron for this experiment, the effects of alloying elements on the final material properties were considered. From these recommendations a final composition was selected which satisfies the property requirements of the infiltration alloy.

First, the infiltration abilities of the white iron alloy must be considered. White iron alloys are typically low in carbon compared to other cast irons, and therefore suffer from poor fluidity. In order for infiltration to be successful, the fluidity of the metal must be improved. This can be accomplished through increased Si content, which improves the fluidity of the alloy [34]. Standard composition ranges for white iron are published by the American Society for Metals (ASM) and are heavily referred to in developing this alloy. High, medium, and low alloying element content is referred to in direct reference to the published content ranges for white iron. [34] Thus, to ensure that the fluidity of the white iron is such that the alloy can easily infiltrate throughout the lattice structure, Si content in the upper ranges of acceptable content was selected.

Next, the Ni and carbon content of the alloy was identified to ensure optimal wear performance. Ideal wear performance in white iron is typically obtained by an iron matrix of heat-treated martensite [34]. For a successful heat treatment without cracking or distortion, it is preferred that the iron matrix be dominated by an as-cast austenitic structure. Because of this, Ni is typically included to inhibit pearlite formation [34]. If pearlite is properly suppressed, the iron matrix becomes super-saturated with carbon and chromium upon cooling and a fully austenitic matrix can be achieved. Although martensite is beneficial for wear resistance, martensite can be brittle and show poor toughness unless properly controlled. Lath martensite is a martensitic structure which features fine grain structure and better toughness than its counterpart, plate martensite. Lower C content favors lath martensite formation and therefore C on the lower end of the acceptable range was selected [35].

High Cr white iron is exceptionally good for abrasion resistance due to the formation of Cr carbide (Cr_7C_3 or $Cr_{23}C_6$). For this reason, high chromium content is essential. Additionally, a gradient between the Cr content of the white iron alloy and the 316L stainless alloy would be desired to foster diffusion across the interface, improving the bonding potential. However, it is important to consider the effects of the carbide formation within the interface of the two materials. Excessive carbon and Cr will diffuse to the grain boundary, leading to carbide precipitation and growth [36]. Carbide formation in the grain boundaries can cause increased sensitization to Intergranular Stress Corrosion Cracking (IGSCC) due to Cr content depletion [37,38].

Alloy ranges typical for high Cr white iron are shown in Table 1. These are obtained from standards published in the ASM Handbook for high alloyed cast irons [34]. Alloy ranges for carbon, silicon, nickel, chromium, and manganese specifically were identified.

Table 1: Recommended alloy ranges for high Cr white iron [34]

	C	Si	Ni	Cr	Mn
Recommended Range (wt%)	2.7-3.6	1.0-1.5	3.4-5.5	9-15	0.8 max

Because impact resistance is important in ground-engaging abrasion resistant components, carbon on the lower end of the acceptable spectrum was selected (2.7 wt% C). Higher Si than typical, 2.0 wt% Si, was chosen to improve the fluidity and ensure complete infiltration of the lattice. 4.8 wt% Ni was chosen due to recommendations from the ASM handbook on pearlite inhibition at large casting thicknesses. Cr on the lower end of the acceptable spectrum was selected due to expected diffusion from the 316L high chromium stainless steel lattice. Lower Cr was additionally selected to drive diffusion across the interface between the high Cr in the stainless steel near 16 wt% and the lower Cr in the white iron near 10%. Lastly, a maximum of 0.8 wt% Mn was allowed as it is an austenite stabilizer and increases as cast austenite. The final selected composition of high Cr white iron is shown in Table 2.

Table 2. Final selected composition for high Cr white iron [34]

	C	Si	Ni	Cr	Mn
Recommended Range (wt%)	2.7	2.0	4.8	10	0.8

Lattice Design

As a tetrakaidecahedron unit cell structure has been identified in prior research as possessing superior strength compared to other unit cell morphologies, it was selected for use in this research [21]. The Lattice Commander module in Autodesk Netfabb was used to convert a 3D solid into a tetrakaidecahedron lattice structure. A relatively small unit cell size of 15mm was selected as the starting point for infiltration examination. A cube was selected as the lattice geometry for infiltration for ease of sectioning, polishing, and observing the face of the component for fusion between the two materials. The cube size was selected to be 60 mm, a multiple of the unit cell size. A rendering of the 15mm unit cell lattice with a 1.5mm strut diameter is shown in Figure 1.

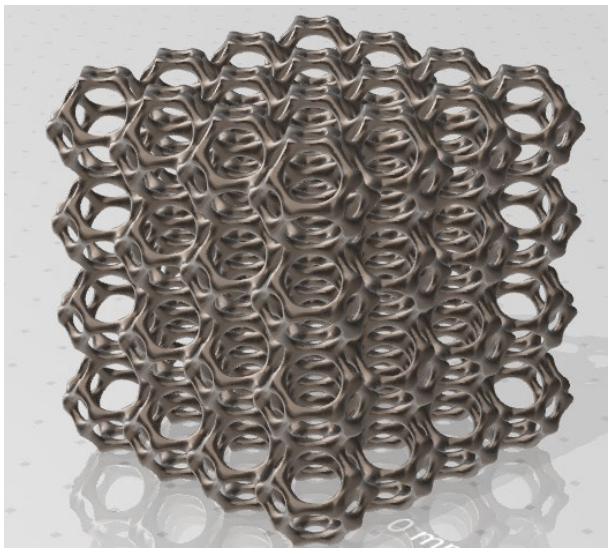

Figure 1: Tetrakaidecahedron lattice developed with Netfabb Lattice Commander

Lattice Fabrication

The lattice structure was printed using a Farsoon FS271M L-PBF System [39]. Supports were not included, as the bottom layer was considered sacrificial and would be cut off when the part was removed from the print bed. The machine was cleaned and then loaded with 316L stainless powder, consisting of a -45+15 particle size distribution and processed through a 200 mesh sieve. The chamber was sealed and preheated to 100°C prior to printing. The chamber was purged with argon to maintain a low oxygen content. General processing parameters used are shown in Table 3. The layer thickness selected provides adequate z-height feature resolution without significantly decreasing print time, while using common power and feeds with rotating hatch directions for SS316L. Multiple lattice structures were printed to ensure the success of the experiment. Upon completion of the print, parts were removed from the substrate using a horizontal bandsaw [39].

Table 3. Processing Parameters used for Fabrication of SS316L Lattice Structures

Processing Parameter Description	*Value*
Layer Thickness	30 µm
Laser Power	225 W
Scan Speed	1000 mm/s
Hatch Distance	0.090 µm

MAGMA Simulation Setup

To ensure optimum filling, MAGMA metal casting simulation software was used to predict the filling/infiltration behavior within the lattice structure. The primary concern with fully infiltrating the lattice with white iron was the lattice acting as a chill, causing the liquid metal to freeze off or loose fluidity before full infiltration. To ensure that a gating design and pouring temperature were selected which would prevent this from occurring, a casting simulation was developed. The effectiveness of a side fill gating design and a top fill gating system design, shown in Figure 2, were explored using MAGMA. It was hypothesized that the side fill design would be better suited to promote smooth filling due to the low turbulence characteristics of the bottom up fill trajectory. Material parameters for high Cr white iron were selected from the MAGMA database for the pouring alloy, and readily available green sand was selected as the mold material. The internal lattice was set to be a steel chill with the material properties selected from an existing MAGMA database; the differences between the standard steel chill and a chill composted of SS316L were considered to be minimal.

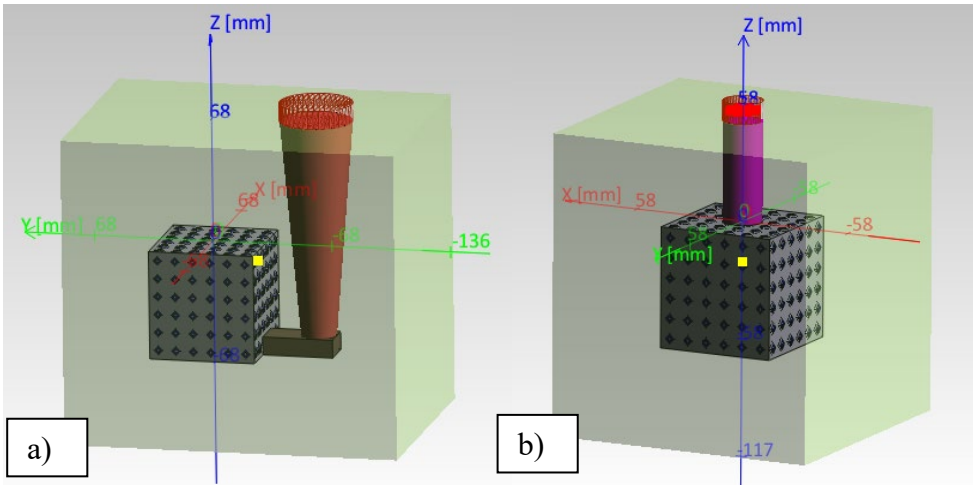

Figure 2. Lattice Infiltration Gating Designs: a) side fill and b) top fill

Pattern Design and Production

Following the adoption of the optimal gating system, a pattern was designed and printed for preparing the mold. A pouring cup and square downsprue system was selected to minimize turbulence in the liquid and to ensure the pouring height remained consistent. A split pattern was designed which featured a 1.5° draft to all sides, allowing for easy mold release. Alignment features were also included for ease of mold making. The gate was modeled based on MAGMA simulation results and was included in the drag side of the split pattern mold. The pattern was 3D printed using a Creality CR-10s Pro FFF printer out of PLA, using a 20% infill to reduce material consumption while maintaining adequate strength to resist compression during molding.

Casting Preparations

Prior to lattice infiltration, a charge table was developed based on materials on hand at Georgia Southern University for the melting of the desired high Cr white iron. The charge table

was designed to account for the raw material chemistries and combined them in such a way that the desired chemistry was achieved. Each material in the table contains a specific weight percent of elemental values that, when combined together, give the desired chemistry of white iron. The charge constituents and their quantities are shown in Table 4.

Table 4: Charge table for selected high Cr white iron chemistry

In charge	*Weight (kg)*	*Weight (lbs)*
Pig Iron	11.5	37.4
1018 Steel	2.43	7.70
FeSi	0.45	1.28
FeMn	0.12	0.40
FeCr	2.6	8.58
Ni	0.86	2.86
Total charge	17.96	39.51

The charge materials were carefully weighted out and added to a 60 lb induction furnace. Next, green sand was prepared for molding. Green sand was mulled and water was added until the compactability reached 45% compaction according to green sand testing equipment. The mold was then prepared as shown in Figure 3. Two cavities were poured to ensure a successful casting was obtained. The iron was poured at 1500 °C. It was first de-slagged and then transferred to a secondary ladle for pouring.

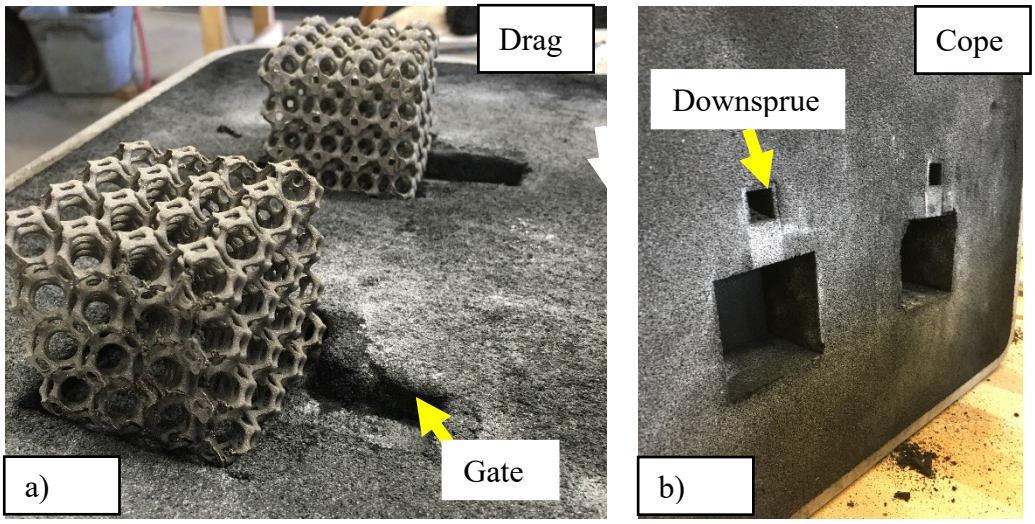

Figure 3: Greensand a) cope and b) drag used to infiltrate lattice with high Cr white iron

Post Processing

After casting, the mold was shaken out. The gating system was removed using a reinforced cut-off wheel mounted on an angle grinder. The casting was sectioned using Wire EDM, as the hardness of the material prevented traditional sectioning methods from being used. A square section showing the interface between the unit cell and the infiltration allow was obtained and mounted as shown in Figure 4. The bottom surface of the sample was ground flat and polished to a 3 μm finish for microscopy. The surface was deep etched with Marbles Reagent to bring out the

carbide phase for imaging. Metallography was then performed on an Olympus BX 53M optical microscope at varying magnifications to examine the diffusion interaction between the materials.

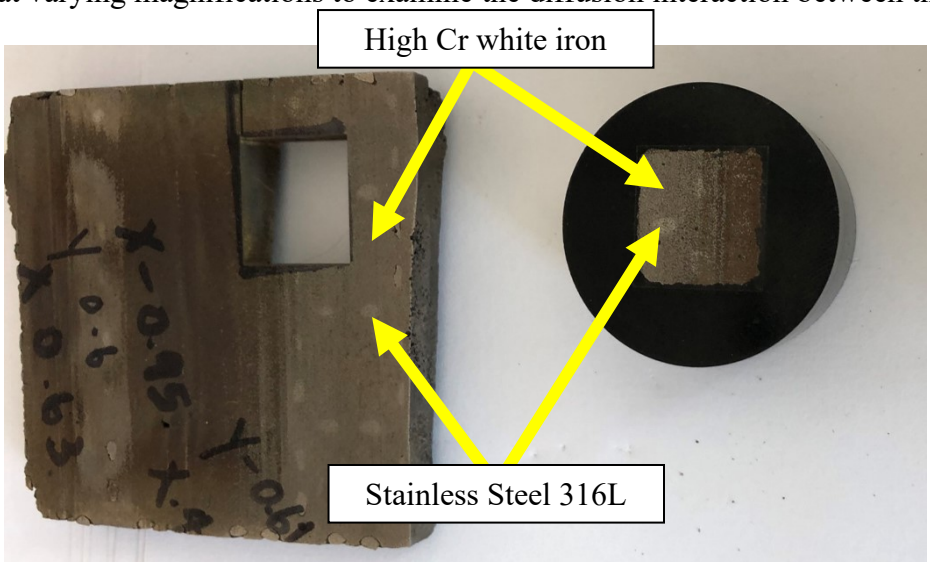

Figure 4: Sample Prepared for Microstructure Analysis

Simulation Results

From the MAGMA simulation results shown in Figure 5, it is clear that the side fill gating system is the more effective means of filling when compared to top fill gating. The top fill method resulted in high turbulence due to the rain-fall type filling around the lattice which drastically increases the risk of defects, oxide formation, and poor bonding. The side fill gating system minimized the overall flow turbulence and promoting smooth filling of the lattice structure. For this reason, the side fill gating system was chosen for the final casting system.

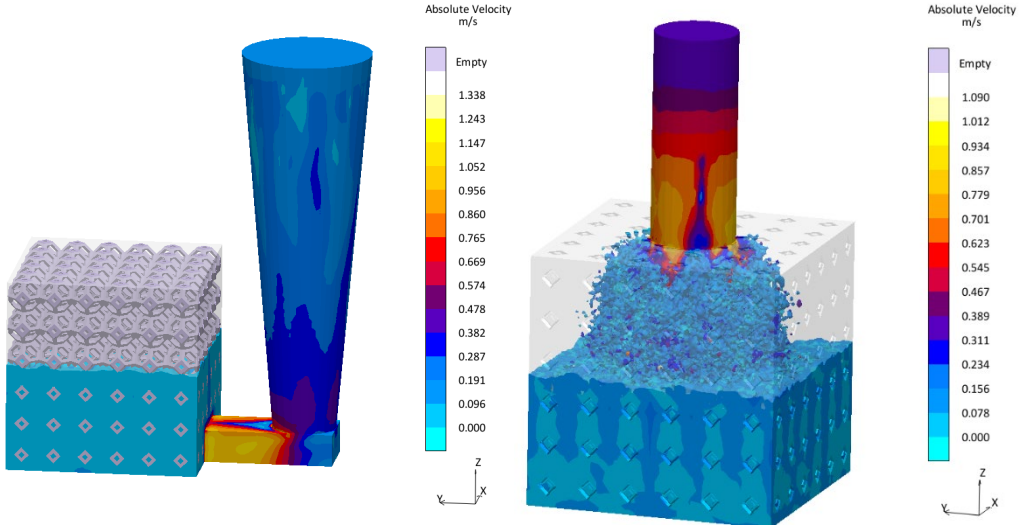

Figure 5: MAGMA Simulation Results Comparing the Two Gating System Designs

Additive Manufactured Lattice Results

The lattice structures printed via L-PBF are shown in Figure 6. The overall print quality of the cell lattice structures appeared to be high, with few defects observed. The surface finish was uniform, although some excessive roughness did occur at the overhang sections. Very few other defects existed, with most occurring at the end of the print due to cumulative damage incurred on the recoater. However, for the purpose of infiltration and fusion studies, all structures were adequate for study.

Figure 6: 316L Stainless Lattice Surface Finish

Casting Quality and Infiltration Results

A final casting after the gating system was removed is shown in Figure 7. The samples were oxidized (scale & ferrous oxide) and had remnants of green sand burn-on. The outside surface finish was not measured but appeared to be slightly rougher due to high pouring temperature. For typical high temperature steel castings, a zircon mold wash is applied to prevent sand-metal interactions, although this is not typically necessary for cast iron. However, since white iron features a lower carbon content than typical cast iron and thus requires a higher pouring temperature, its interaction with the greensand mold material was similar to that of steel castings, and a mold wash would have been beneficial to improve the surface finish. As casting surface quality is not critical to the success of the infiltration experiment, the castings were overall deemed to be successful. Scale and ferrous oxide were removed from the areas of interest using sand blasting and grinding before sectioning for microscopy.

Figure 7: As-Cast 316L Stainless Steel Lattice Infiltrated with high Cr white iron

Chemistry Analysis

Samples taken from the gating systems of the castings were used for elemental analysis through optical spectroscopy to determine the final as-cast chemistry. An Amtek SPECTROMAXx spectrometer calibrated based on "type correction" standards was used to burn the samples and obtain the actual chemistry. Three burns were made, and the results were averaged. The resulting chemistry according to the spectrometer reading is shown in Table 5 and compared with the target chemistry.

Table 5: Target versus Actual Composition

	TARGET COMPOSITION (WT%)	ACTUAL COMPOSITION (WT%)	PERCENT ERROR (%)
C	2.7	2.8	3.7
SI	2.0	2.11	5.5
NI	4.8	4.25	11.5
CR	10	9.84	1.6
MN	0.8	0.82	2.5

Using this measured chemistry, a solidification diagram was generated using the JMat Pro Chemistry Analysis software and is shown in Figure 8. The solidification diagram gives information as to what phases will be present in the final as-cast microstructure. As seen in the diagram, the final microstructure will feature an austenitic matrix with carbide and cementite phases.

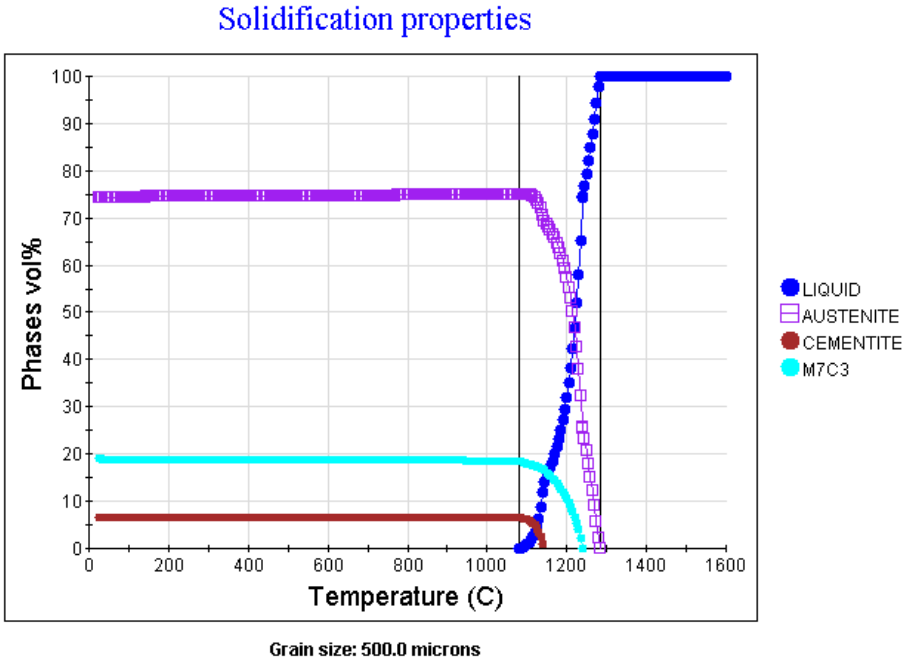

Figure 8: Solidification diagram generated for the actual white iron chemistry

Microstructure Analysis

Following the polishing and etching of the bimetal composite interface, metallographic images were taken at varying magnifications. The high Cr white iron microstructure was examined and is shown in Figure 9.

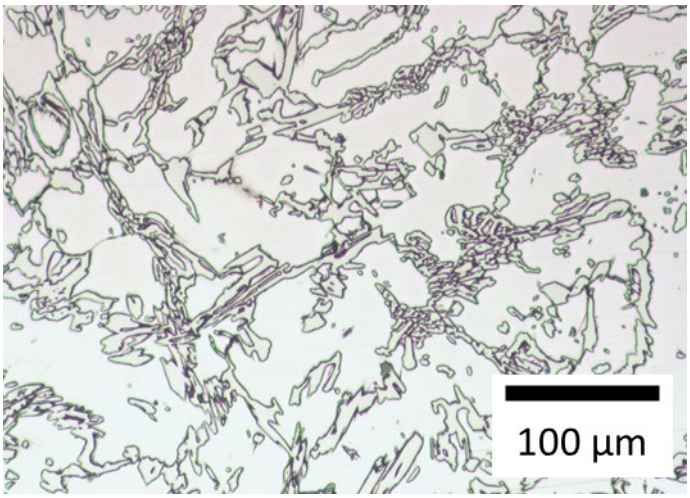

Figure 9: Medium magnification image of the white iron microstructure

Medium and high magnification images of the fusion zone between the stainless steel lattice and high Cr white iron are shown in Figure 10.

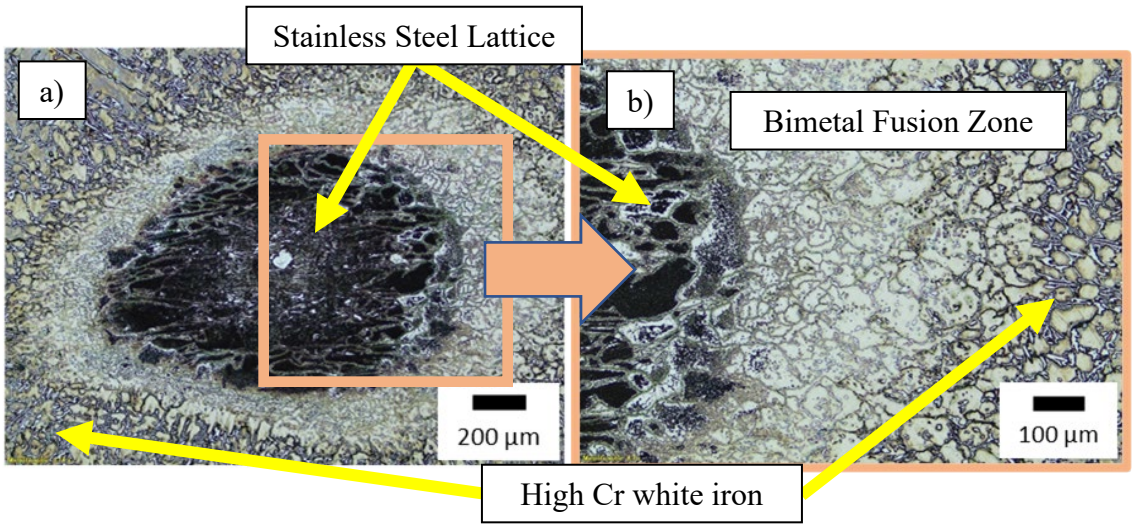

Figure 10: a) Medium and b) high magnification image of carbide growth along the grain boundary in the bimetal fusion zone

In examining the microstructure of the high Cr white iron, extensive carbide formation is observed in the white iron. Figure 9 resolves the Cr carbide network through an austenitic matrix. This is expected based on the solidification diagram generated by JMat Pro thermal analysis software shown in Figure 8. Additionally, the microstructure shown in Figure 10(b) at the bimetal interface shows carbide precipitating out along the grain boundary of the stainless steel austenitic microstructure. This grain boundary carbide precipitation indicates diffusion along the interface between the two alloys.

Figure 10 also shows an example of complete fusion between the AM lattice structure and the cast white iron. As can be seen, complete metallurgical bonding was achieved with little if any porosity, inclusions, or other defects. This was observed throughout the interior of the cast samples.

Although throughout the interior of the structure complete metallurgical bonding was observed, incomplete fusion did occur at the outer walls of the sample. Along the outer bounds of the bimetallic structure, at the interface between the two alloys, complete fusion was not observed. Distinct separation of the lattice and high Cr white iron matrix did occur in some places, as shown in Figure 11.

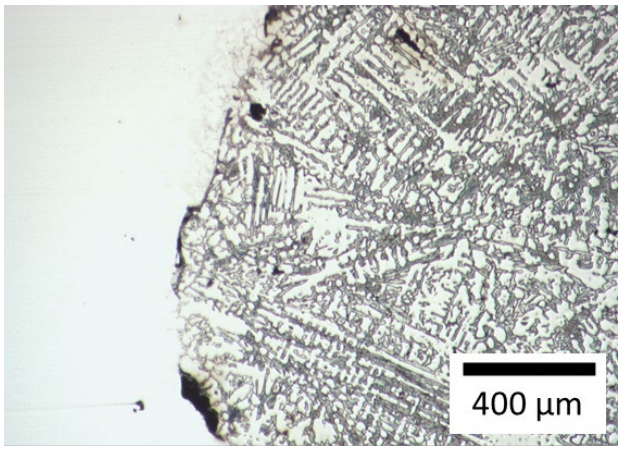

Figure 11. Separation of the stainless steel lattice and high Cr white iron along the outer bounds of the structure

The incomplete bonding observed at the surface of the sample is likely due to contact with the mold wall. Effective bonding between the two alloys is the function of heat and time. Due to heat transfer away from the structure to the mold wall, the interior of the sample had more time for fusion at temperature as compared to the outer surface. Although incomplete fusion was observed at the surface of the sample, complete infiltration of the lattice at these locations resulted in a firm mechanical fit between the two materials.

Through this casting process, a bimetallic composite structure was achieved through both metallurgical and mechanical bonding of two materials. Through the implementation of an AM lattice structure, brittle white iron was reinforced by a ductile stainless steel lattice structure, successfully resulting in a reinforced bimetallic wear component.

Future Work

In order to further quantify the effects of integrating stainless steel 316L with high Cr white iron, the authors propose to investigate both mechanical and microstructural properties. EDS analysis across the fusion zone will enable a full gradient of Cr depletion and carbide formation along the grain boundary. Previous studies have shown that carbide precipitation is less for large grain microstructures, and greater for small grain microstructures [38], therefore, characterization of grain size will qualitatively support the EDS analysis. Furthermore, micro hardness testing will provide a gradient of micro-scale mechanical properties across the fusion zone while fatigue and quasi-static testing will enable macro-scale properties. Simulated mechanics models will be compared against the experimental results and adjusted accordingly. Additionally, the starting chemistry and molding techniques can be altered in light of the current results to promote diffusion and control carbide morphology, leading to solid solution strengthening.

Conclusions

A method has been introduced in which high abrasion resistant alloys such as high Cr white iron may be reinforced through the application of AM techniques. It is shown that a stainless steel lattice structure produced through L-PBF may be infiltrated with high Cr white iron to produce a

reinforced bimetallic wear component. It was observed that complete lattice infiltration was possible, and a mixed bimetal interface was observed featuring fused and unfused interface zones. The metallurgically bonded interface region featured chromium diffusion from the AM lattice structure which formed chromium carbides along the interface between the two materials. This research shows that high Cr white iron may be used to infiltrate an additively manufactured stainless steel lattice structure for producing a reinforced wear component.

References

[1] El-Aziz, K. A., and Saber, D., 2020, "Mechanical and Microstructure Characteristics of Heat-Treated of High-Cr WI and AISI4140 Steel Bimetal Beams," J. Mater. Res. Technol., **9**(4), pp. 7926–7936.

[2] Wróbel, T., 2014, "Characterization of Bimetallic Castings with an Austenitic Working Surface Layer and an Unalloyed Cast Steel Base," J. Mater. Eng. Perform., **23**(5), pp. 1711–1717.

[3] Rong, S. F., Zhao, X. M., Zhou, H. T., Wang, J. F., Yao, J., and Li, C. H., 2014, "Study on Coated-Liquid-Liquid Trimetal Composite Casting Hammer," Mater. Res. Innov., **18**(5), pp. S2316–S2322.

[4] Bhadeshia, H., and Honeycombe, R., 2017, "Iron-Carbon Equilibrium and Plain Carbon Steels," *Steels: Microstructure and Properties*, Elsevier, Cambridge.

[5] Zhu, Y. chang, Wei, Z. jie, Rong, S. fan, Wang, H. wei, and Zou, C. ming, 2016, "Formation Mechanism of Bimetal Composite Layer between LCS and HCCI," China Foundry, **13**(6), pp. 396–401.

[6] Zic, S., Dzambas, I., and Ikonic, M., 2009, "Possibilities of Implimenting Bimetallic Hammer Castings in Crushing Industries," **48**(1), pp. 51–54.

[7] Wróbel, T., 2011, "Ni AND Cr BASE LAYERS IN BIMETALLIC CASTINGS," Mater. 20th Anniv. Int. Conf. Metall. Mater. – Met. 2011., pp. 758–764.

[8] Ramadan, M., 2018, "Interface Structure and Elements Diffusion of As-Cast and Annealed Ductile Iron/Stainless Steel Bimetal Castings," Eng. Technol. Appl. Sci. Res., **8**(2), pp. 2709–2714.

[9] Wróbel, T., and Szajnar, J., 2015, "Bimetallic Casting: Ferritic Stainless Steel - Grey Cast Iron," Arch. Metall. Mater., **60**(3B), pp. 2361–2365.

[10] Pan, Y. N., Chang, W. S., and Chang, R. M., 2008, "Optimal Heat Treatment Conditions and Properties of Bimetal (High Cr Cast Iron/Alloyed Steel) Hammers," Int. J. Cast Met. Res., **21**(1–4), pp. 71–75.

[11] Wan, J., Qing, J., and Xu, M., 2019, "Designing a Novel Graphitic White Iron for Metal-to-Metal Wear Systems," Metall. Mater. Trans. A Phys. Metall. Mater. Sci., **50**(3), pp. 1162–1174.

[12] Hans, B., and Werner, T., 2008, *Ferrous Materials*, Springer-Verlag, Leipzig.

[13] Bandyopadhyay, A., Zhang, Y., and Bose, S., 2020, "Recent Developments in Metal Additive Manufacturing," Curr. Opin. Chem. Eng., **28**, pp. 96–104.

[14] Hassen, A. A., Noakes, M., Nandwana, P., Kim, S., Kunc, V., Vaidya, U., Love, L., and Nycz, A., 2020, "Scaling Up Metal Additive Manufacturing Process to Fabricate Molds for Composite Manufacturing," Addit. Manuf., **32**(March 2019), p. 101093.

[15] Chen, N., Khan, H. A., Wan, Z., Lippert, J., Sun, H., Shang, S. L., Liu, Z. K., and Li, J., 2020, "Microstructural Characteristics and Crack Formation in Additively Manufactured Bimetal Material of 316L Stainless Steel and Inconel 625," Addit. Manuf., **32**(December 2019), p. 101037.

[16] Williams, C. B., Cochran, J. K., and Rosen, D. W., 2011, "Additive Manufacturing of Metallic Cellular Materials via Three-Dimensional Printing," Int. J. Adv. Manuf. Technol., **53**(1–4), pp. 231–239.

[17] Yan, C., Hao, L., Hussein, A., Bubb, S. L., Young, P., and Raymont, D., 2014, "Evaluation of Light-Weight AlSi10Mg Periodic Cellular Lattice Structures Fabricated via Direct Metal

Laser Sintering," J. Mater. Process. Technol., **214**(4), pp. 856–864.
[18] Yan, C., Hao, L., Hussein, A., and Raymont, D., 2012, "Evaluations of Cellular Lattice Structures Manufactured Using Selective Laser Melting," Int. J. Mach. Tools Manuf., **62**, pp. 32–38.
[19] Chu, C., Graf, G., and Rosen, D. W., 2008, "Design for Additive Manufacturing of Cellular Structures," Comput. Aided. Des. Appl., **5**(5), pp. 686–696.
[20] Lv, W., Li, D., and Dong, L., 2020, "Study on Mechanical Properties of a Hierarchical Octet-Truss Structure," Compos. Struct., **249**(January), p. 112640.
[21] Zhong, T., He, K., Li, H., and Yang, L., 2019, "Mechanical Properties of Lightweight 316L Stainless Steel Lattice Structures Fabricated by Selective Laser Melting," Mater. Des., **181**, p. 108076.
[22] Alzahrani, M., Choi, S. K., and Rosen, D. W., 2015, "Design of Truss-like Cellular Structures Using Relative Density Mapping Method," Mater. Des., **85**, pp. 349–360.
[23] Wang, Y., Li, S., Yu, Y., Xin, Y., Zhang, X., Zhang, Q., and Wang, S., 2020, "Lattice Structure Design Optimization Coupling Anisotropy and Constraints of Additive Manufacturing," Mater. Des., **196**, p. 109089.
[24] Tam, K.-M. M., 2015, "Principal Stress Line Computation for Discrete Topology Design."
[25] Zhao, M., Zhang, D. Z., Liu, F., Li, Z., Ma, Z., and Ren, Z., 2020, "Mechanical and Energy Absorption Characteristics of Additively Manufactured Functionally Graded Sheet Lattice Structures with Minimal Surfaces," Int. J. Mech. Sci., **167**(October 2019).
[26] Surmeneva, M. A., Surmenev, R. A., Chudinova, E. A., Koptioug, A., Tkachev, M. S., Gorodzha, S. N., and Rännar, L. E., 2017, "Fabrication of Multiple-Layered Gradient Cellular Metal Scaffold via Electron Beam Melting for Segmental Bone Reconstruction," Mater. Des., **133**, pp. 195–204.
[27] Yang, J., Jin, X., Gao, H., Zhang, D., Chen, H., Zhang, S., and Li, X., 2020, "Additive Manufacturing of Trabecular Tantalum Scaffolds by Laser Powder Bed Fusion: Mechanical Property Evaluation and Porous Structure Characterization," Mater. Charact., **170**(July), p. 110694.
[28] Vangapally, S., Agarwal, K., Sheldon, A., and Cai, S., 2017, "Effect of Lattice Design and Process Parameters on Dimensional and Mechanical Properties of Binder Jet Additively Manufactured Stainless Steel 316 for Bone Scaffolds," Procedia Manuf., **10**, pp. 750–759.
[29] Burr, A., Persenot, T., Doutre, P. T., Buffiere, J. Y., Lhuissier, P., Martin, G., and Dendievel, R., 2020, "A Numerical Framework to Predict the Fatigue Life of Lattice Structures Built by Additive Manufacturing," Int. J. Fatigue, **139**(June), p. 105769.
[30] Greitemeier, D., Palm, F., Syassen, F., and Melz, T., 2017, "Fatigue Performance of Additive Manufactured TiAl6V4 Using Electron and Laser Beam Melting," Int. J. Fatigue, **94**, pp. 211–217.
[31] Anand, M., and Das, A. K., 2021, "Issues in Fabrication of 3D Components through DMLS Technique : A Review," Opt. Laser Technol., **139**(February 2020), p. 106914.
[32] Simchi, A., and Asgharzadeh, H., 2004, "Densification and Microstructural Evaluation during Laser Sintering of M2 High Speed Steel Powder," Mater. Sci. Technol., **20**(11), pp. 1462–1468.
[33] "316/316L Stainless Steel."
[34] Gundlach, R. B., 2018, "White Iron and High-Alloyed Iron Castings," Casting, **200**(c), pp. 896–903.
[35] Bhadeshia, H. K. D. ., and Honeycombe, R. W. ., 2017, *Steels: Microstructure and*

Properties, Elsevier, Cambridge.
[36] Cao, T., Cheng, C., Ye, F., Xv, H., and Zhao, J., 2020, "Relationship between Carbon Segregation and the Carbide Precipitation along Grain Boundary Based on the Structural Unit Model," J. Mater. Sci., pp. 7883–7893.
[37] Yin, Y., Faulkner, R. G., Moreton, P., Armson, I., and Coyle, P., 2010, "Grain Boundary Chromium Depletion in Austenitic Alloys," J. Mater. Sci., **45**(21), pp. 5872–5882.
[38] Li, S. X., Li, L., Yu, S. R., Akid, R., and Xia, H. B., 2011, "Investigation of Intergranular Corrosion of 316L Stainless Steel Diffusion Bonded Joint by Electrochemical Potentiokinetic Reactivation," Corros. Sci., **53**(1), pp. 99–104.
[39] "FS271M Farsoon," ANIWAA [Online]. Available: https://www.aniwaa.com/product/3d-printers/farsoon-fs271m/. [Accessed: 01-May-2021].